Check for updates

Forced and spontaneous symmetry breaking in cell polarization

Pearson W. Miller [1,8], Daniel Fortunato [2,8], Cyrill Muratov [3,4 ✉], Leslie Greengard [2,5 ✉] and Stanislav Shvartsman [1,5,6,7 ✉]

How does breaking the symmetry of an equation alter the symmetry of its solutions? Here, we systematically examine how reducing underlying symmetries from spherical to axisymmetric influences the dynamics of an archetypal model of cell polarization, a key process of biological spatial self-organization. Cell polarization is characterized by nonlinear and non-local dynamics, but we overcome the theory challenges these traits pose by introducing a broadly applicable numerical scheme allowing us to efficiently study continuum models in a wide range of geometries. Guided by numerical results, we discover a dynamical hierarchy of timescales that allows us to reduce relaxation to a purely geometric problem of area-preserving geodesic curvature flow. Through application of variational results, we analytically construct steady states on a number of biologically relevant shapes. In doing so, we reveal non-trivial solutions for symmetry breaking.

The very first action undertaken in all of geometry is, per Euclid, 'to draw a straight line from any point to any point'[1]. We would be hard pressed to achieve the precise spatial organization observed in cellular biology without an established directional axis. Cells may assign direction through the process of polarization, in which they break internal symmetry by sequestering signaling proteins from the cytosol to a specific region (the polar cap) of the cell membrane. The importance of understanding this mechanism is underscored by its ubiquity: cell polarity establishes directions of locomotion and growth, mechanical anisotropies and planes of division[2–6]. A wide range of molecular factors are known to influence spontaneous polarization, including complex intracellular regulatory networks, mechanical cues and external chemical gradients[7,8]. In this Article, we demonstrate how a cell's own shape can directly determine cell polarization outcomes.

The biological role played by cell shape has drawn substantial attention from theorists, but firm quantitative results have proved elusive because of the mathematical difficulties of coupling nonlinear chemical dynamics to non-trivial surface geometry. Several studies have explored the reduced scenario of a two-dimensional cell bounded by a one-dimensional membrane[5,7,9], or simplified network representations[10]. Previous numerical studies with fully three-dimensional embedded cell membranes have been restricted to simpler shapes such as spheres or spheroids[11–13]. Nonetheless, recent papers have reported numerical results hinting at general rules for polarization on more general cell shapes, such as a tendency of polar cap drift towards regions of high curvature, or, alternatively, for polarization to occur along the longest axis of a given cell[14–17].

Our goal in this paper is to propose a computational method to assess such intuitive claims via the following question: given a cell membrane of axisymmetric (rather than spherical) shape, what are the possible stable, symmetry-broken distributions of membrane-bound proteins? This is a matter of forced, rather than spontaneous, symmetry breaking, which limits deployment of traditional methods

such as the equivariant branching lemma[18]. Instead, we approach this problem through exhaustive simulation, exploring geometric effects robustly over a range of realistic cell shapes. To this end, we introduce a variant of the double Fourier sphere (DFS) method[19–21] for fast and accurate simulation of nonlinear, non-local partial differential equations on surfaces of revolution. Our initial numerical results suggest that steady states are close to solutions to the isoperimetric problem on the surface of the cell. Further numerical experiments clarify previously suggested rules for geometry-guided cell polarization and construct counterexamples highlighting where these break down.

Results

Model derivation. A prototypical cell polarity model consists of a three-dimensional domain Ω enclosed by a surface $\partial\Omega$ with normal vector $\mathbf{n}$ and a single chemical species that is located either on the boundary or within the bulk (Fig. 1a). The simplest model with spontaneous symmetry breaking has three important characteristics: conservation of total mass, bulk diffusion substantially faster than lateral membrane diffusion, and cooperative reaction kinetics governing binding and unbinding from the cell membrane. A substantial library of polarization models exhibit these features[22,23], but for the purposes of this paper we focus on a simple wave-pinning system, so called because its dynamics feature the arrested motion of a traveling wavefront[24]. It captures the essence of several real systems, such as ezrin polarization in embryonic mouse cells[5], and can be written as

$$\partial_t B = D_B \nabla^2_{\partial\Omega} B + k_b \left(\beta + \frac{B^\nu}{G^\nu + B^\nu} \right) C - k_d B, \tag{1}$$

$$\partial_t C = D_C \nabla^2_\Omega C, \tag{2}$$

$$D_C (\nabla C \cdot \mathbf{n})|_{\partial\Omega} = -k_b \left(\beta + \frac{B^\nu}{G^\nu + B^\nu} \right) C + k_d B. \tag{3}$$

¹Center for Computational Biology, Flatiron Institute, New York, NY, USA. ²Center for Computational Mathematics, Flatiron Institute, New York, NY, USA. ³Department of Mathematical Sciences, New Jersey Institute of Technology, Newark, NJ, USA. ⁴Dipartimento di Matematica, Università di Pisa, Pisa, Italy. ⁵Courant Institute, New York University, New York, NY, USA. ⁶Department of Molecular Biology, Princeton University, Princeton, NJ, USA. ⁷Lewis-Sigler Institute for Integrative Genomics, Princeton University, Princeton, NJ, USA. ⁸These authors contributed equally: Pearson W. Miller, Daniel Fortunato. ✉e-mail: muratov@njit.edu; lgreengard@flatironinstitute.org; stas@princeton.edu
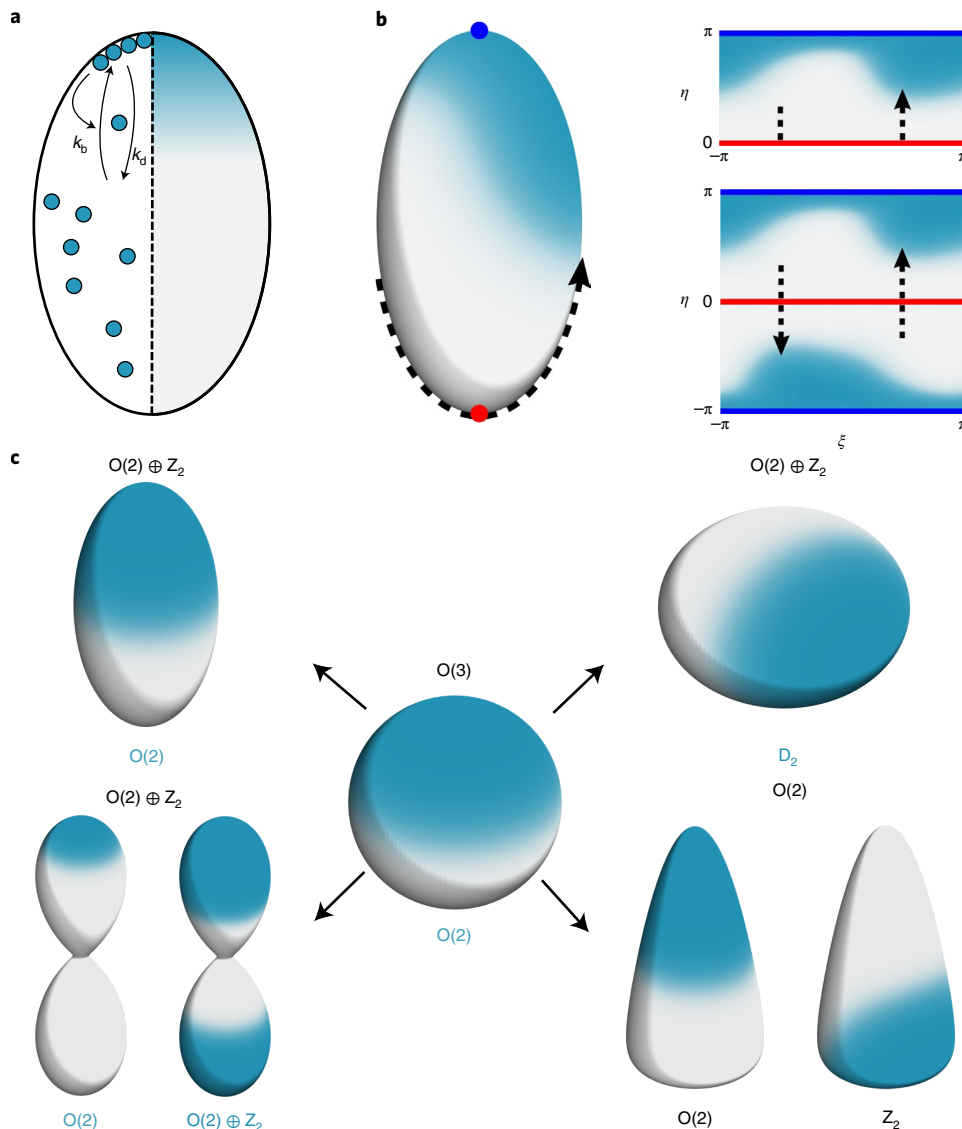
Fig. 1 | Dynamics of cell polarization. a, Cytosolic proteins autocatalytically bind to the cell membrane nonlinearly and undergo slow lateral diffusion, leading to spontaneous symmetry breaking on the surface in vivo. **b**, Natural periodicity across the poles is lost when a function is represented using on-surface coordinates (ξ, η). The DFS method recovers this periodicity by reflecting and shifting the function, allowing computations to be carried out using two-dimensional Fourier series. **c**, Steady-state behavior exhibits non-trivial dependence on surface geometry. Some surfaces even admit multiple classes of solution. Text in black denotes the symmetry group of the surface, text in blue the symmetry of the steady-state solution.

Here, (1) describes a reaction–diffusion process on $\partial\Omega$ of the surface-bound concentration B, while (2) gives bulk diffusion of C in the bounded volume Ω and (3) the boundary condition between the two. The operator $\nabla_{\partial\Omega}^2$ is the Laplace–Beltrami operator on the surface, while ∇_Ω^2 refers to the standard three-dimensional Laplacian. D_B and D_C are the diffusion constants on the membrane and in the cytosol, respectively. The parameter k_d represents a constant rate of unbinding from the membrane, while k_b is the corresponding rate of binding. The term inside the parentheses represents a small basal binding β and a cooperative binding given by a Hill function, which is characterized by a characteristic concentration G and Hill coefficient ν. The wave-pinning dynamics we describe below does not strongly depend on ν, so throughout our simulations will use $\nu = 2$. These equations leave considerable room for simplification under our assumptions. As mass is conserved globally, we define the quantity C_{tot} as the total mass divided by bulk volume $|\Omega|$. Under the assumption that $D_B \ll D_C$, we can treat

the bulk concentration as spatially uniform and study a reduced system determined entirely by surface dynamics[25]. Thanks to conservation of mass, we can write

$$C = C_{tot} - \frac{1}{|\Omega|} \int_{\partial\Omega} B \, dS.$$

Substituting this back into (1) yields the reduced equation for surface-bound species,

$$\frac{\partial B}{\partial t} =$$
$$D_B \nabla_{\partial\Omega}^2 B - k_d B + k_b \left(\beta + \frac{B^\nu}{G^\nu + B^\nu} \right) \left(C_{tot} - \frac{1}{|\Omega|} \int_{\partial\Omega} B \, dS \right).$$

This result can be rendered dimensionless by rescaling as $\tau = k_d t$, $u = k_d B / (k_b C_{tot})$ and $ds = dS / |\partial\Omega|$, where $|\partial\Omega|$ is the surface area of $\partial\Omega$, to non-dimensionalize the equation as

$$\frac{\partial u}{\partial \tau} = \delta^2 \nabla^2_{\partial\Omega} u - u + \left(\beta + \frac{u^\nu}{\gamma^\nu + u^\nu} \right) \left(1 - \alpha \int_{\partial\Omega} u \, ds \right), \quad (4)$$

with dimensionless parameters $\delta^2 = D_B/(k_d|\partial\Omega|)$, $\alpha = k_b|\partial\Omega|/(2k_d|\Omega|)$ and $\gamma = k_d G/(k_b C_{tot})$. The spontaneous symmetry breaking of this equation on a sphere has been carefully studied, providing a strong starting point for discussions of less-symmetric surfaces[11]. A brief discussion of results on alternative polarization models can be found in Supplementary Information as well as in Supplementary Fig. 4 and Supplementary Table 1.

Modified DFS for axisymmetric surfaces. To numerically represent functions on $\partial\Omega$, we modify the classical DFS method for use on any closed surface of revolution. The DFS method maps a function on $\partial\Omega$ to a rectangular longitude–latitude coordinate system (ξ, η) that is 'doubled up' in such a way as to preserve the natural periodicity of the function both azimuthally and across the poles (Fig. 1b). Such a biperiodic representation permits the use of bivariate Fourier series to approximate the membrane-bound concentration u on $\partial\Omega$. To stably evolve equation (4), we discretize in time with an implicit–explicit scheme that treats the surface diffusion term implicitly in Fourier space and the nonlinear, non-local reaction term explicitly in grid space. Hence, at each time step we must invert a modified Laplace–Beltrami operator of the form $\mathcal{I} - c\nabla^2_{\partial\Omega}$, where $\mathcal{I}$ is the identity operator and $c > 0$. Fortunately, upon discretizing $\mathcal{I} - c\nabla^2_{\partial\Omega}$ with bivariate Fourier series, the azimuthal modes decouple; this holds true for any surface of revolution. Moreover, as both differentiation and band-limited multiplication are sparse operations on Fourier coefficients, the modified Laplace–Beltrami problem can be discretized into a set of decoupled, banded linear systems—one for each azimuthal Fourier mode—which may be solved in parallel. The DFS method gives us a fast $\mathcal{O}(mn)$ algorithm for inverting the modified Laplace–Beltrami operator on surfaces of revolution, yielding an overall cost per time step of $\mathcal{O}(mn \log mn)$ operations for $m \times n$ Fourier coefficients. For $m = n = 128$, the solver takes approximately 0.02 s when run on a single core; using eight cores reduces the solve time to 0.006 s. For the simulations presented throughout this work, using $m = n = 64$ or 128 was sufficient to achieve a maximum relative error of 10^{-8} when compared with an over-resolved solution. The code for our scheme is open source and available online[26,27]. For a detailed description of the numerical method, see Methods and Supplementary Figs. 1–3. Simulations of the cell polarization model in equation (4) on several sample surfaces are presented in Supplementary Video 1.

The initial results shown in Fig. 1c highlight the scope of our problem. For ease of comparison, we note the symmetry group of the surfaces (black) and solutions (blue). Surfaces with the same underlying symmetries are found to admit radically different solutions: the prolate and oblate spheroids are symmetric to rotation about their axes and reflection about the equator (in group theory parlance, they share the symmetry group denoted $O(2) \bigoplus Z_2$; see ref. [28] for definitions). However, the solutions of the former are symmetric under axial rotations (symmetry group $O(2)$) while the latter's solutions remain invariant under horizontal and vertical reflection (D_2). Indeed, the bottom row demonstrates that the same surface can admit multiple, qualitatively different classes of solutions. The hourglass-shaped surface admits both one- and two-cap steady states, while the conical surface allows both axisymmetric ($O(2)$) and off-center (Z_2) solutions. To make sense of these disparate examples, we take a closer look at the dynamics of the polarization process.

Asymptotic hierarchy of timescales. Extensive simulation reveals three distinct dynamical timescales, similar to the cascade of timescales reported in ref. [29], in the biologically relevant slow-diffusion regime where dimensionless diffusion $\delta \ll 1$ (Fig. 2a) for a surface
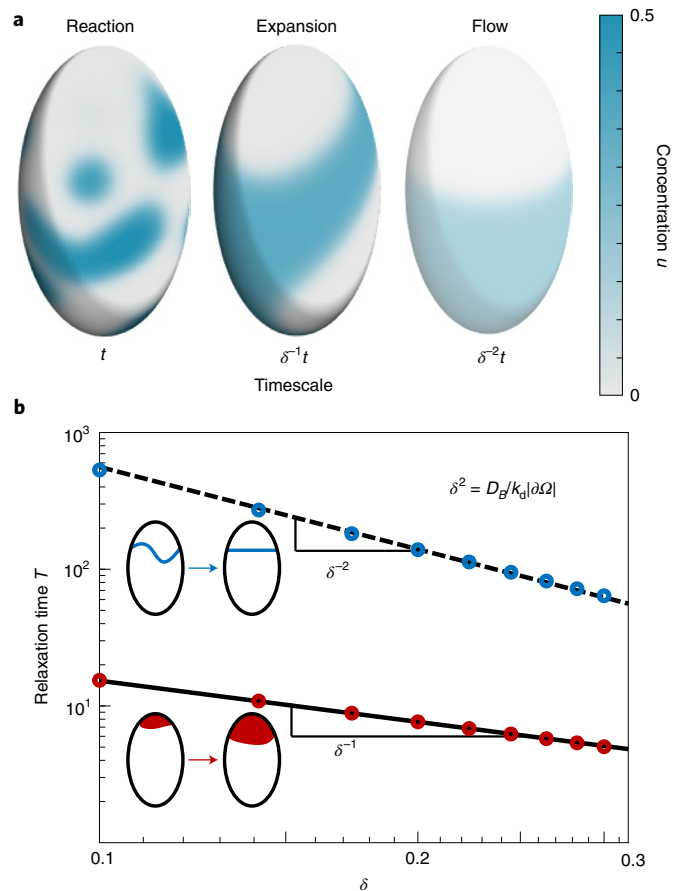

Fig. 2 | Pattern formation over a hierarchy of timescales. a, Snapshots of the polarization dynamics at each characteristic timescale. On the fast timescale $\mathcal{O}(1)$, time evolution is purely local via the reaction kinetics, which drive the phase separation of high- and low-density membrane regions. At the intermediate timescale $\mathcal{O}(\delta^{-1})$, the initially random distribution evolves towards a cap with fixed area. Finally, over the long timescale $\mathcal{O}(\delta^{-2})$, interface minimization drives the migration of the cap over the surface. **b**, Starting from a small, localized perturbation from a uniform concentration profile, the times needed for the interface to reach to within 1% of its maximum cap area (red) and final interface length (blue) are calculated over a range of δ. Both cases exhibit clear power-law scaling with δ at the reported exponents. Simulations were performed with $\alpha = 3$, $\beta = 0$, $\nu = 2$, $\gamma = 0.2$.

area $|\partial\Omega|$. With lateral diffusion slowed, initial dynamics are dominated entirely by the bulk-membrane binding kinetics, leading to rapid local relaxation at each point on the surface. We observe that the total mass of the membrane-bound protein converges to a fixed value, causing the solution to grow or shrink from initial conditions to a fixed area fraction of the total membrane surface. Tracking the time needed for area to converge, we find it scales as δ^{-1} (Fig. 2b, red). While this target area depends on the surface area to volume ratio of the cell, it is independent of local geometry. On long timescales, it has been hypothesized that dynamics on the scale of δ^{-2} are driven by minimization of the length of the interface between high- and low-concentration regions bounding the cap[30-32]. Conceptually, this interface minimization emerges from the high dissipative cost of maintaining the interface in the face of the inherently high protein fluxes in this region. This cost should scale linearly with the length of the interface, and ergo the boundary can be thought of as possessing an effective line tension in the long-time limit[15].
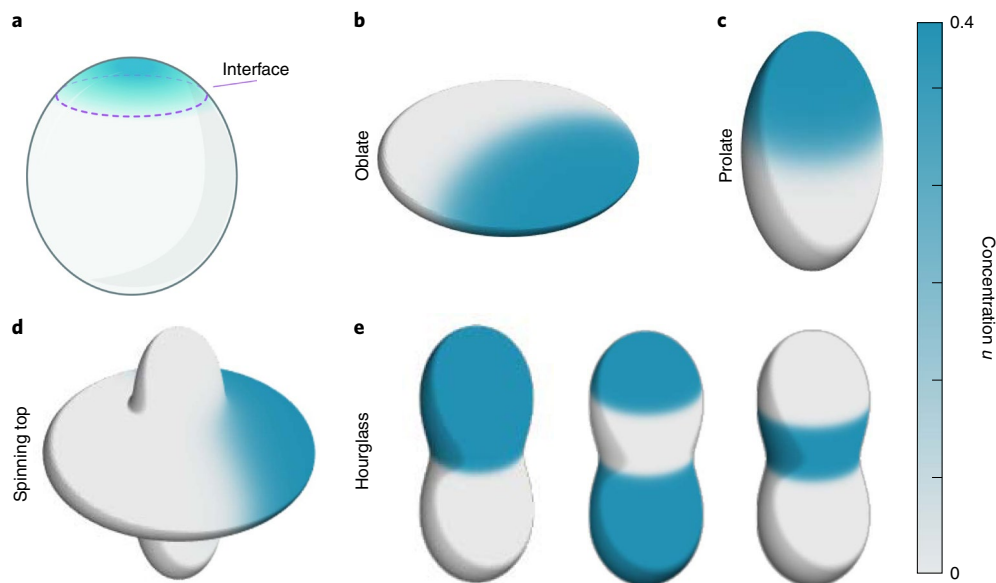
Fig. 3 | Geometric effects on cap localization. a, Steady-state solutions minimize the length of the interface between high- and low-concentration regions. **b**, Oblate spheroids only have stable caps centered on equatorial points. **c**, A stable cap on the prolate spheroid is axisymmetric and centered on the pole. **d**, For this cap size, a stable solution exists centered on the rim of this spinning top shape, but not about the local maximum of Gaussian curvature at the pole. **e**, Surfaces with negative Gaussian curvature can admit a number of solutions, including multiple stable caps and solutions where high concentration does not localize to high positive curvature.

Given a fixed enclosed area, area-preserving geodesic curvature flow naturally arises out of interface minimization[33]. In particular, if we define $\Gamma(t) = \{u(\cdot, t) = \gamma\}$, the γ level-set of $u(x, t)$ at time t, then under a sharp-interface approximation (Fig. 3a) we expect that the normal velocity v_n of Γ can be written as

$$v_n = k_g - \langle k_g \rangle, \tag{5}$$

in which k_g and $\langle k_g \rangle$ are the local and mean geodesic curvatures of Γ, respectively. We tracked the length of said interface over our simulations and found that the time needed for it to steady does indeed scale as δ^{-2}, establishing a third and final timescale (Fig. 2b, blue). This scaling behavior is entirely consistent with geodesic curvature flow in other non-local, conservative systems[34]. Crucially, equation (5) reflects the well known fact that minimal curves exhibit constant geodesic curvature.

Thus, to find stable steady-state solutions, we must find caps of fixed area but locally minimal interfaces. Before proceeding to specific cases, it is important to note a general existence result: for an arbitrary compact surface, there exists an area-constrained minimizer of perimeter for any given area, whose boundary takes the form of a union of smooth closed curves sharing a common, uniform k_g. Proof of this follows from standard arguments in the calculus of variations[35]. In the context of cell polarization, we interpret this result as implying that no plausible cell geometry will inherently restrict symmetry breaking. Polarization can always occur, and the question simply becomes where, as we now discuss.

Calculations of steady-state solutions. As noted above, the general qualitative notion is that the polar cap partitions the cell along its long axis, or alternatively stabilizes at the peak of Gaussian curvature. We examine these claims for surfaces of revolution, making use of the fact that stable solutions of the isoperimetric problem have been fully classified for surfaces that are symmetric to reflections over the plane of their equator[36–38]. When Gaussian curvature K is everywhere positive, matters are relatively simple. If K is increasing with distance from the poles, as in the oblate spheroid, stable solutions can only exist centered on the equatorial points (Fig. 3b). Conversely, shapes such as the prolate spheroid where curvature increases monotonically away from the equator always exhibit an axisymmetric symmetry at the poles (Fig. 3c). For these cases, then, the popular rule of thumb holds. Similar results are discussed for other polarization models in Supplementary Information (Supplementary Fig. 4).

Expanding our range to surfaces with negative Gaussian curvature, however, reveals previously unacknowledged complexity. Adding dimples of negative K at the poles of the oblate spheroid changes nothing: only equator-centered solutions are allowed for these shapes[37]. However, consider the transition from the prolate spheroid to the hourglass-shaped surface presented in Fig. 3e, reminiscent of a cell undergoing division. The analog of the solution on the prolate spheroid, an axisymmetric cap centered at the pole, remains intact. However, variational solutions of the constrained perimeter-minimization problem reveal that two interface solutions also exist. For instance, for an appropriately chosen area, one can find a solution with two interfaces of curvature k_g symmetric with respect to the equator provided that they are contained within the region $K + k_g^2 < 0$. Up to a choice of parameters, this leads to two new axisymmetric solutions: one equator centered, and one with two caps. Thus, we find caps that do not partition the shape in two, and one that even avoids high-curvature regions entirely. For surfaces where variational solutions are not available—such as the spinning top shape (Fig. 3d)—we can use simulation to find stable cap configurations. Here we observe that polarization can occur on either the rim or the pole depending on cap size. Such solutions bear some similarity to those found for binary alloy models[38].

As noted above, plausible cell shapes tend to support multiple polar cap solutions. However, biology often requires one particular solution to be favored over others; pyramid-shaped embryonic mouse cells, for instance, must polarize to their outer surface. As a final exercise, we use our numerical scheme to test selection between distinct steady states on an egg-shaped surface that resembles a blastomere in an eight-cell mouse embryo (Fig. 4)[5]. Understanding the mechanisms that guide polarization in these
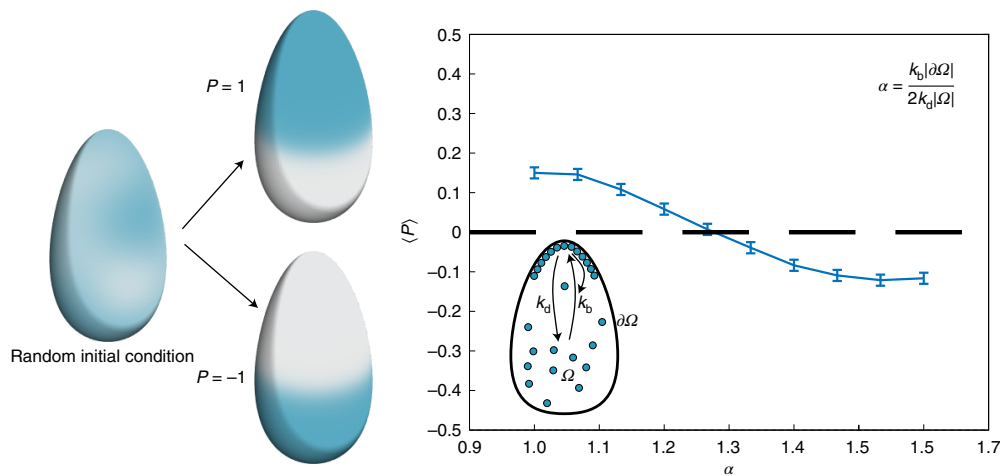
Fig. 4 | Polarity selection on asymmetric surfaces. Polarity establishment on an egg-shaped surface of revolution is examined when simulations are time-evolved from a small random perturbation about a uniform steady state. Left: for a given simulation, we assign a value $P = \pm 1$ depending on whether the polar cap goes to the sharp or blunt end of the egg. Right: we examine how polarization is influenced by α by plotting the mean value of P across $n = 5,000$ simulations at each value of α. Error bars denote 1 s.d. above and below this mean as calculated from the same set of simulations.

cells is a major open problem in mammalian developmental biology, with several competing hypotheses currently at play. Starting from random initial conditions slightly perturbed from the uniform unstable steady state, we investigate whether polarization favors the top or bottom of the surface as a function of α. This test is equivalent to an experiment modulating the cap size by over- or underexpressing enzymes controlling binding and unbinding to the surface. In vivo, the mouse cell always forms its polar cap on its blunt side, and yet on the basis of the previous section we might expect the cap to favor the side of the egg with sharper curvature. Contrary to both hypotheses, after 5,000 trials per data point we only record a relatively small bias whose direction could be tuned by the value of α. We interpret this result as an indication that, while geometry establishes possible cap locations, it does not play a major role is selecting between them (Supplementary Video 2). Looking at it another way, these results seem to indicate that geometry plays too small a selective role to account for the robustness of orientation selection seen in the embryo, suggesting that alternative mechanisms must be at work.

Our results establish a systematic overview of geometry-forced symmetry breaking for axisymmetric surfaces, highlighting prototypical cases where the common sense understanding holds and where it fails. By carefully examining the results of numerical simulations, we were able to identify a cascade of pattern-forming timescales. We exploited the purely geometric nature of the long-timescale dynamics to establish a number of unambiguous properties about symmetry breaking, and demonstrated the distinction in symmetry-breaking polarization between classes of axisymmetric surfaces exemplified by prolate and oblate spheroids. Further, we constructed clear counterexamples illustrating the breakdown of the high-curvature localization rule. It remains an open question how far these results extend to the case of finite bulk diffusion, though existing results suggest that even this regime is guided by interface minimization on long timescales[15,39].

Discussion

In this Article, we have illustrated how shape influences symmetry in one particular cell polarization model related to the Rho–GTP pathway, but the general question of how intracellular signaling reacts to geometric guiding cues remains a rich and active area of research. As noted in Supplementary Information, our numerical code is well suited to the study of other mechanisms of cell polarization

problems in a range of other molecular contexts, such as the Rac–Rho pathway or CDC-42. Recent work has also highlighted the role of geometry in cell polarization at the tissue scale, offering another avenue for future work[40]. Beyond cell polarization, biology provides a host of other problems in need of efficient methods to study reaction–diffusion on surfaces. For example, surface-bound Rho–GTP dynamics in starfish oocytes is emerging as a popular experimental system for the study of spiral waves and active turbulence[41,42]. Recent evidence suggests that geometry plays a major role in guiding this reaction–diffusion system[39]. Simultaneously, numerical studies of turbulent behavior in this system benefit immensely from the use of spectral methods, making this an obvious application for DFS[43].

The DFS method developed here can also be generalized to other problems beyond reaction–diffusion. It is a fairly straightforward exercise in geometry to calculate higher-order spatial derivatives in the same way as the Laplace–Beltrami operator. A DFS-based calculation of the surface biharmonic operator, for example, would be an extremely efficient way to study mechanical problems on axisymmetric domains. Once again, biology motivates a wide range of problems that would be suited to this. Models of actively deforming cell membranes, for example, generally require higher-order derivatives and are a major subject of interest in contexts such as cellular locomotion or division[44,45]. Biologically realistic cell deformation, for instance due to actomyosin contraction, is often analytically intractable and numerically expensive, creating a pressing need for numerical methods such as ours in this area[46].

While the modified DFS method developed here performs well in the simple geometries considered in this work, it has its limitations. First, the DFS method is notably limited to axisymmetric surfaces. On the other hand, traditional mesh-based solvers such as the finite-element method (FEM) are applicable to general surfaces. However, what the DFS method lacks in generality it makes up for in speed by exploiting axisymmetry. In comparison with a second-order accurate subdivision FEM implemented in libMesh (version 1.5.1)[47], our solver achieves an orders of magnitude speedup (Supplementary Fig. 3 and the corresponding discussion in Supplementary Information). Second, as the DFS method is a spectral method, it provides global resolution of functions on the surface with no opportunity for spatial adaptivity. While spectral methods can achieve exponential convergence for smooth functions, they suffer when the solution possesses a discontinuity or is not globally smooth. Adaptive mesh-based methods may perform better than a

global spectral method when applied to reaction–diffusion systems where smoothness is not guaranteed.

Methods

The Laplace–Beltrami operator on axisymmetric surfaces. Let $\partial\Omega$ be a smooth, axisymmetric, closed surface of genus zero embedded in $\mathbb{R}^3$. Let $(\rho(\xi,\eta), \lambda(\xi,\eta), \theta(\xi,\eta)) \in [0,\infty] \times [-\pi,\pi] \times [0,\pi]$ be a smooth parametrization of $\partial\Omega$ in spherical coordinates with $(\xi,\eta) \in [-\pi,\pi] \times [0,\pi]$ denoting on-surface longitude and colatitude. Note that λ is the azimuthal angle and θ is the polar angle. Axisymmetry requires such a parametrization to have the form $(\rho(\xi,\eta), \lambda(\xi,\eta), \theta(\xi,\eta)) = (\rho(\eta), \xi, \theta(\eta))$; in other words, an axisymmetric surface is entirely defined through its generating curve $(\rho(\eta), \theta(\eta))$. Converting this representation to Cartesian coordinates $\mathbf{x}(\xi,\eta) = (x(\xi,\eta), y(\xi,\eta), z(\xi,\eta))$, we have

$$x(\xi,\eta) = \rho(\eta)\sin\theta(\eta)\cos\xi, \; y(\xi,\eta)$$
$$= \rho(\eta)\sin\theta(\eta)\sin\xi, \; z(\xi,\eta) = \rho(\eta)\cos\theta(\eta).$$

The metric tensor g on $\partial\Omega$ is then given by

$$g = \begin{bmatrix} g_{\xi\xi} & g_{\xi\eta} \\ g_{\eta\xi} & g_{\eta\eta} \end{bmatrix} = \begin{bmatrix} \mathbf{x}_\xi \cdot \mathbf{x}_\xi & \mathbf{x}_\xi \cdot \mathbf{x}_\eta \\ \mathbf{x}_\eta \cdot \mathbf{x}_\xi & \mathbf{x}_\eta \cdot \mathbf{x}_\eta \end{bmatrix},$$

where $\mathbf{x}_\xi = \partial\mathbf{x}/\partial\xi$ and $\mathbf{x}_\eta = \partial\mathbf{x}/\partial\eta$. Let the components of the inverse of g be denoted by

$$g^{-1} = \begin{bmatrix} g^{\xi\xi} & g^{\xi\eta} \\ g^{\eta\xi} & g^{\eta\eta} \end{bmatrix} = \frac{1}{|g|}\begin{bmatrix} g_{\eta\eta} & -g_{\xi\eta} \\ -g_{\eta\xi} & g_{\xi\xi} \end{bmatrix},$$

with $|g| = \det g$. The surface gradient of a scalar-valued function $u = u(\xi,\eta)$ defined on $\partial\Omega$ can then be written as

$$\nabla_{\partial\Omega} u = \left(g^{\xi\xi}\frac{\partial u}{\partial\xi} + g^{\xi\eta}\frac{\partial u}{\partial\eta}\right)\mathbf{x}_\xi + \left(g^{\eta\xi}\frac{\partial u}{\partial\xi} + g^{\eta\eta}\frac{\partial u}{\partial\eta}\right)\mathbf{x}_\eta.$$

Similarly, the surface divergence of a vector field $\mathbf{u} = \mathbf{u}(\xi,\eta) = u_1(\xi,\eta)\mathbf{x}_\xi + u_2(\xi,\eta)\mathbf{x}_\eta$ tangent to $\partial\Omega$ can be written as

$$\nabla_{\partial\Omega} \cdot \mathbf{u} = \frac{1}{\sqrt{|g|}}\left(\frac{\partial}{\partial\xi}\left(\sqrt{|g|}\, u_1\right) + \frac{\partial}{\partial\eta}\left(\sqrt{|g|}\, u_2\right)\right).$$

Therefore, the Laplace–Beltrami operator on $\partial\Omega$ is given by

$$\nabla^2_{\partial\Omega} u = \nabla_{\partial\Omega} \cdot \nabla_{\partial\Omega} u$$
$$= \frac{1}{\sqrt{|g|}}\left(\frac{\partial}{\partial\xi}\sqrt{|g|}\left(g^{\xi\xi}\frac{\partial u}{\partial\xi} + g^{\xi\eta}\frac{\partial u}{\partial\eta}\right) + \frac{\partial}{\partial\eta}\sqrt{|g|}\left(g^{\eta\xi}\frac{\partial u}{\partial\xi} + g^{\eta\eta}\frac{\partial u}{\partial\eta}\right)\right)$$
$$= \frac{1}{\sqrt{|g|}}\left(\frac{\partial}{\partial\xi}\frac{1}{\sqrt{|g|}}\left(g_{\eta\eta}\frac{\partial u}{\partial\xi} - g_{\xi\eta}\frac{\partial u}{\partial\eta}\right) + \frac{\partial}{\partial\eta}\frac{1}{\sqrt{|g|}}\left(g_{\xi\xi}\frac{\partial u}{\partial\eta} - g_{\eta\xi}\frac{\partial u}{\partial\xi}\right)\right).$$

For our axisymmetric surface $\partial\Omega$, we have that

$$\mathbf{x}_\xi = \begin{bmatrix} -\rho\sin\theta\sin\xi \\ \rho\sin\theta\cos\xi \\ 0 \end{bmatrix}, \qquad \mathbf{x}_\theta = \begin{bmatrix} \rho'\sin\theta\cos\xi + \rho\cos\theta\,\theta'\cos\xi \\ \rho'\sin\theta\sin\xi + \rho\cos\theta\,\theta'\sin\xi \\ \rho'\cos\theta - \rho\sin\theta\,\theta' \end{bmatrix},$$

and so the metric tensor is given by

$$g = \begin{bmatrix} \rho^2\sin^2\theta & 0 \\ 0 & \rho^2\theta'^2 + \rho'^2 \end{bmatrix},$$

with $|g| = \rho^2\sin^2\theta\,(\rho^2\theta'^2 + \rho'^2)$. Therefore, the Laplace–Beltrami operator on $\partial\Omega$ is

$$\nabla^2_{\partial\Omega} u = \frac{g_{\eta\eta}}{|g|}\frac{\partial^2 u}{\partial\xi^2} + \frac{g_{\xi\xi}}{|g|}\frac{\partial^2 u}{\partial\eta^2} + \left(\frac{g_{\xi\xi}}{|g|}\frac{\partial}{\partial\eta}\left(\frac{1}{\sqrt{|g|}}\right) + \frac{1}{|g|}\frac{\partial}{\partial\eta}\left(g_{\xi\xi}\right)\right)\frac{\partial u}{\partial\eta}$$
$$= \frac{1}{\rho^2\sin^2\theta}\frac{\partial^2 u}{\partial\xi^2} + \frac{1}{\rho^2\theta'^2 + \rho'^2}\frac{\partial^2 u}{\partial\eta^2} + \left[\frac{\rho'^3 - \rho^3\theta'\theta'' - \rho\rho'\rho''}{\rho(\rho^2\theta'^2 + \rho'^2)^2} + \frac{\theta'\cos\theta}{\sin\theta(\rho^2\theta'^2 + \rho'^2)}\right]\frac{\partial u}{\partial\eta}.$$

Numerical methods. The dimensionless cell polarization model on $\partial\Omega$ is a nonlinear, non-local partial differential equation of the form

$$\frac{\partial u}{\partial\tau} = \mathcal{L}u + \mathcal{N}(u), \qquad (6)$$

with $\mathcal{L}u = \delta^2\nabla^2_{\partial\Omega} u$ and $\mathcal{N}(u) = (\beta + \frac{u^\nu}{\gamma^\nu + u^\nu})(1 - \alpha\int_{\partial\Omega} u\,\mathrm{d}S) - u$. We discretize (6) using the DFS method in space and an implicit–explicit scheme in time.

For a smooth function $u(x,y,z)$ on $\partial\Omega$, the parametrization $u(\xi,\eta)$ is periodic in ξ but not in η. To obtain a biperiodic function using the DFS method, we 'double up' u so that

$$\tilde{u}(\xi,\eta) = \begin{cases} u(\xi,\eta), & (\xi,\eta) \in [-\pi,\pi] \times [0,\pi], \\ u(\xi+\pi,-\eta) & (\xi,\eta) \in [-\pi,0] \times [-\pi,0], \\ u(\xi-\pi,-\eta) & (\xi,\eta) \in [0,\pi] \times [-\pi,0]. \end{cases}$$

The function $\tilde{u}(\xi,\eta)$ may then be discretized using a bivariate $m \times n$ Fourier series,

$$\tilde{u}(\xi,\eta) \approx \sum_{j=-m/2}^{m/2-1}\sum_{k=-n/2}^{n/2-1} \tilde{U}_{jk}\, e^{ij\eta}\, e^{ik\xi}, \qquad (\xi,\eta) \in [-\pi,\pi]^2,$$

and computations on $\tilde{u}(\xi,\eta)$ may be related back to the original function $u(\xi,\eta)$.

We use an implicit–explicit scheme to stably evolve (6) in time, with the linear term $\mathcal{L}u$ treated implicitly and the nonlinear term $\mathcal{N}(u)$ treated explicitly. Fix a step size $\Delta\tau > 0$ and time points $\tau_k = k\,\Delta\tau$ for integers $k \geq 0$, and let $\tilde{u}^k$ denote the DFS approximation to the solution to (6) at time τ_k. Using the fourth-order backward differentiation formula scheme (we start this multistep scheme using three steps of the fourth-order linearly implicit Runge–Kutta method LIRK4[48]) in time yields a steady-state partial differential equation for $\tilde{u}^{k+1}$,

$$(25\mathcal{I} - 12\,\Delta\tau\,\mathcal{L})\tilde{u}^{k+1} = 48\tilde{u}^k - 36\tilde{u}^{k-1} + 16\tilde{u}^{k-2} - 3\tilde{u}^{k-3} + \Delta\tau$$
$$\left(48\mathcal{N}(\tilde{u}^k) - 72\mathcal{N}(\tilde{u}^{k-1}) + 48\mathcal{N}(\tilde{u}^{k-2}) - 12\mathcal{N}(\tilde{u}^{k-3})\right), \qquad (7)$$

which must be solved once per time step to compute $\tilde{u}^{k+1}$ from $\{\tilde{u}^k, \tilde{u}^{k-1}, \tilde{u}^{k-2}, \tilde{u}^{k-3}\}$. Here, $\mathcal{I}$ is the identity operator and we evaluate the nonlinear term pseudospectrally, which requires one forward and one inverse two-dimensional fast Fourier transform to be performed at a cost of $\mathcal{O}(mn\log mn)$ operations per time step. Specifically, we evaluate the nonlinear term as

$$\mathcal{N}(\tilde{u}) \approx \mathrm{fft2}(\mathcal{N}_{\mathrm{pseudo}}(\mathrm{ifft2}(\tilde{U})))\,\mathcal{N}_{\mathrm{spec}}(\tilde{U}) - \tilde{U},$$

where fft2 and ifft2 denote the forward and inverse two-dimensional fast Fourier transforms, $\mathcal{N}_{\mathrm{pseudo}}(\tilde{u}) = \beta + \frac{\tilde{u}^\nu}{\gamma^\nu + \tilde{u}^\nu}$ and $\mathcal{N}_{\mathrm{spec}}(\tilde{U}) = 1 - \alpha\sum_{j=-m/2}^{m/2} w_j\tilde{U}_{j0}$ with precomputed weights $w_j = \int_0^\pi e^{ij\eta}\rho\sin\theta\sqrt{\rho^2\theta'^2 + \rho'^2}\,\mathrm{d}\eta$ for $-m/2 \leq j \leq m/2$. Equation (7) takes the form of a modified Laplace–Beltrami problem, $\mathcal{L}\tilde{u} - c^2\tilde{u} = f$, for some $c \in \mathbb{R}$ and smooth function f on $\partial\Omega$.

A fast modified Laplace–Beltrami solver for axisymmetric surfaces. We now aim to develop a solver for the modified Laplace–Beltrami problem on $\partial\Omega$,

$$\nabla^2_{\partial\Omega} u - c^2 u = f, \qquad (8)$$

where f is a smooth function on $\partial\Omega$ and $c \in \mathbb{R}$. For our axisymmetric surface $\partial\Omega$, (8) becomes

$$A(\eta)\frac{\partial^2 u}{\partial\eta^2} + B(\eta)\frac{\partial u}{\partial\eta} + C(\eta)\frac{\partial^2 u}{\partial\xi^2} - D(\eta)c^2 u = D(\eta)f, \qquad (9)$$

for $(\xi,\eta) \in [-\pi,\pi] \times [0,\pi]$, where

$$A(\eta) = \rho^2\sin^2\theta\,(\rho^2\theta'^2 + \rho'^2),$$
$$B(\eta) = \rho\sin^2\theta\,(\rho'^3 - \rho^3\theta'\theta'' - \rho\rho'\rho'') + \rho^2\sin\theta\,(\rho^2\theta'^2 + \rho'^2)\,\theta'\cos\theta,$$
$$C(\eta) = (\rho^2\theta'^2 + \rho'^2)^2,$$
$$D(\eta) = \rho^2\sin^2\theta(\rho^2\theta'^2 + \rho'^2)^2.$$

Let $\tilde{u}$ and $\tilde{f}$ be the doubled-up versions of u and f, respectively, and define the functions

$$\tilde{A}(\eta) = \begin{cases} A(\eta), & \eta \in [0,\pi], \\ A(-\eta), & \eta \in [-\pi,0], \end{cases} \qquad \tilde{B}(\eta) = \begin{cases} B(\eta), & \eta \in [0,\pi], \\ -B(-\eta), & \eta \in [-\pi,0], \end{cases}$$

$$\tilde{C}(\eta) = \begin{cases} C(\eta), & \eta \in [0,\pi], \\ C(-\eta), & \eta \in [-\pi,0], \end{cases} \qquad \tilde{D}(\eta) = \begin{cases} D(\eta), & \eta \in [0,\pi], \\ D(-\eta), & \eta \in [-\pi,0]. \end{cases}$$

These functions are 2π periodic, globally smooth for $\eta \in [-\pi,\pi]$, and equal to the functions $A(\eta)$, $B(\eta)$, $C(\eta)$ and $D(\eta)$ for $\eta \in [0,\pi]$. Then the governing equation for $\tilde{u}$ is given by

$$\tilde{A}(\eta)\frac{\partial^2 \tilde{u}}{\partial \eta^2} + \tilde{B}(\eta)\frac{\partial \tilde{u}}{\partial \eta} + \tilde{C}(\eta)\frac{\partial^2 \tilde{u}}{\partial \xi^2} - \tilde{D}(\eta)c^2\tilde{u} = \tilde{D}(\eta)\tilde{f}, \tag{10}$$

for $(\xi, \eta) \in [-\pi, \pi]^2$, which is equivalent to (9) when $\tilde{u}$ is restricted to the original domain $[-\pi, \pi] \times [0, \pi]$.

We discretize (10) using the Fourier spectral method in two dimensions, which represents the functions $\tilde{u}$ and $\tilde{f}$ as matrices of bivariate Fourier coefficients $\tilde{U}, \tilde{F} \in \mathbb{C}^{m \times n}$. Let $D_m \in \mathbb{C}^{m \times m}$ and $D_n \in \mathbb{C}^{n \times n}$ be diagonal Fourier differentiation matrices and $M_{\tilde{A}}, M_{\tilde{B}}, M_{\tilde{C}}, M_{\tilde{D}} \in \mathbb{C}^{m \times m}$ be Fourier multiplication matrices for the univariate functions $\tilde{A}, \tilde{B}, \tilde{C}$ and $\tilde{D}$. For smooth geometries, these functions are band limited and can be represented using q Fourier coefficients with $q \ll \max(m, n)$, thus making their Fourier multiplication matrices q banded. Upon discretizing (10), we obtain the matrix equation

$$\left(M_{\tilde{A}} D_m^2 + M_{\tilde{B}} D_m - c^2 M_{\tilde{D}}\right) \tilde{U} + M_{\tilde{C}} \tilde{U} D_n^2 = M_{\tilde{D}} \tilde{F}. \tag{11}$$

Since D_n is a diagonal matrix, (11) decouples column-wise and each column of $\tilde{U}$ —which represents a fixed azimuthal mode—can be found independently by solving a separate $m \times m$ banded linear system,

$$\left(M_{\tilde{A}} D_m^2 + M_{\tilde{B}} D_m - c^2 M_{\tilde{D}} + M_{\tilde{C}}(D_n^2)_{kk}\right) \tilde{U}_{:,k} = M_{\tilde{D}} \tilde{F}_{:,k}, \tag{12}$$

for $-n/2 \leq k \leq n/2 - 1$. Thus, solving the modified Laplace–Beltrami problem amounts to solving n banded linear systems of size $m \times m$, at a total cost of $\mathcal{O}(mn)$.

Convergence and benchmarking. To demonstrate convergence and stability of the overall method, we performed both spatial and temporal self-convergence studies on a prolate spheroid with major axis 1.44 and minor axis 0.77 and parameters $\delta^2 = 0.02$, $\alpha = 2$, $\beta = 0.01$, $\gamma = 0.23$ and $\nu = 2$. To measure convergence in space, we first computed a reference solution at time $\tau = 10$ using an over-refined expansion of 512×512 Fourier coefficients and a time step of $\Delta\tau = 0.05$, starting from random initial conditions for which polarization occurs. Then, we ran simulations from the same initial conditions using smaller values of $m = n$ and measured the maximum pointwise relative error at $\tau = 10$ between the reference and computed solutions. We observe superalgebraic spatial convergence—that is, convergence at a rate of $\mathcal{O}(\rho^{-n})$ with $\rho > 1$—to the reference solution (Supplementary Fig. 1).

To measure convergence in time, we computed a reference solution at time $\tau = 10$ using an over-refined time step of $\Delta\tau = 2^{-8} \approx 0.004$ and an expansion of 64×64 Fourier coefficients, again starting from random initial conditions. We then ran simulations from the same initial conditions using larger values of $\Delta\tau$ and measured the maximum pointwise relative error at $\tau = 10$ between the reference and computed solutions. We observe fourth-order convergence in time (Supplementary Fig. 2).

Finally, we benchmarked our DFS method against a second-order accurate subdivision FEM implemented in libMesh[47,49]. To do this, we ran simulations for 1,000 time steps over a range of modal sizes (using DFS) and mesh sizes (using FEM) and recorded the computation time and error compared with a reference solution. Supplementary Figure 3 shows the relative error versus computation time for both methods. While the FEM requires minutes to achieve three-digit accuracy, our DFS method achieves 12-digit accuracy in a matter of seconds. It is worth noting that the FEM simulations here use an explicit forward Euler method in time, while our DFS method uses the implicit scheme described previously. Using a similar implicit scheme in the FEM simulations would likely increase the cost per time step and widen the gap between the methods seen in Supplementary Fig. 3.

Reporting summary. Further information on research design is available in the Nature Research Reporting Summary linked to this article.

Data availability
Source data for all quantitative results are available with this manuscript and on Zenodo[50].

Code availability
The code for our scheme is open source and an implementation in MATLAB (R2021a) is available on both GitHub[26] and Zenodo[27]. This code is licensed under the MIT license.

References
1. Heath, T. L. et al. *The Thirteen Books of Euclid's Elements* (Courier, 1956).
2. Gross, P. et al. Guiding self-organized pattern formation in cell polarity establishment. *Nat. Phys.* **15**, 293–300 (2019).
3. Mietke, A., Jemseena, V., Kumar, K. V., Sbalzarini, I. F. & Jülicher, F. Minimal model of cellular symmetry breaking. *Phys. Rev. Lett.* **123**, 188101 (2019).
4. Brauns, F. et al. Bulk–surface coupling identifies the mechanistic connection between Min-protein patterns in vivo and in vitro. *Nat. Commun.* **12**, 3312 (2021).
5. Zhu, M. et al. Developmental clock and mechanism of de novo polarization of the mouse embryo. *Science* **370**, eabd2703 (2020).
6. Chen, W., Nie, Q., Yi, T.-M. & Chou, C.-S. Modelling of yeast mating reveals robustness strategies for cell–cell interactions. *PLoS Comput. Biol.* **12**, e1004988 (2016).
7. Rappel, W.-J. & Edelstein-Keshet, L. Mechanisms of cell polarization. *Curr. Opin. Syst. Biol.* **3**, 43–53 (2017).
8. Tostevin, F., Wigbers, M., Søgaard-Andersen, L. & Gerland, U. Four different mechanisms for switching cell polarity. *PLoS Comput. Biol.* **17**, e1008587 (2021).
9. Goryachev, A. B. & Leda, M. Many roads to symmetry breaking: molecular mechanisms and theoretical models of yeast cell polarity. *Mol. Biol. Cell* **28**, 370–380 (2017).
10. Thalmeier, D., Halatek, J. & Frey, E. Geometry-induced protein pattern formation. *Proc. Natl Acad. Sci. USA* **113**, 548–553 (2016).
11. Diegmiller, R., Montanelli, H., Muratov, C. B. & Shvartsman, S. Y. Spherical caps in cell polarization. *Biophys. J.* **115**, 26–30 (2018).
12. Bäcker, J. P. & Röger, M. Analysis and asymptotic reduction of a bulk-surface reaction-diffusion model of Gierer-Meinhardt type. *Commun. Pure Appl. Math.* **21**, 1139 (2022).
13. Gamba, A., Kolokolov, I., Lebedev, V. & Ortenzi, G. Universal features of cell polarization processes. *J. Stat. Mech. Theory Exp.* **2009**, P02019 (2009).
14. Cusseddu, D., Edelstein-Keshet, L., Mackenzie, J. A., Portet, S. & Madzvamuse, A. A coupled bulk–surface model for cell polarisation. *J. Theor. Biol.* **481**, 119–135 (2019).
15. Geßele, R., Halatek, J., Würthner, L. & Frey, E. Geometric cues stabilise long-axis polarisation of PAR protein patterns in *C. elegans*. *Nat. Commun.* **11**, 539 (2020).
16. Rätz, A. & Röger, M. Symmetry breaking in a bulk–surface reaction–diffusion model for signalling networks. *Nonlinearity* **27**, 1805 (2014).
17. Trogdon, M. et al. The effect of cell geometry on polarization in budding yeast. *PLoS Comput. Biol.* **14**, e1006241 (2018).
18. Golubitsky, M., Stewart, I. & Schaeffer, D. G. *Singularities and Groups in Bifurcation Theory: Volume II* (Applied Mathematical Sciences Vol. 69, Springer, 2012).
19. Merilees, P. E. The pseudospectral approximation applied to the shallow water equations on a sphere. *Atmosphere* **11**, 13–20 (1973).
20. Orszag, S. A. Fourier series on spheres. *Mon. Weather Rev.* **102**, 56–75 (1974).
21. Townsend, A., Wilber, H. & Wright, G. B. Computing with functions in spherical and polar geometries I. The sphere. *SIAM J. Sci. Comput.* **38**, C403–C425 (2016).
22. Goryachev, A. B. & Pokhilko, A. V. Dynamics of cdc42 network embodies a Turing-type mechanism of yeast cell polarity. *FEBS Lett.* **582**, 1437–1443 (2008).
23. Otsuji, M. et al. A mass conserved reaction–diffusion system captures properties of cell polarity. *PLoS Comput. Biol.* **3**, e108 (2007).
24. Mori, Y., Jilkine, A. & Edelstein-Keshet, L. Wave-pinning and cell polarity from a bistable reaction–diffusion system. *Biophys. J.* **94**, 3684–3697 (2008).
25. Sharma, V. & Morgan, J. Global existence of solutions to reaction–diffusion systems with mass transport type boundary conditions. *SIAM J. Math. Anal.* **48**, 4202–4240 (2016).
26. Fortunato, D. Spectral methods for reaction–diffusion on axisymmetric surfaces. *GitHub* https://github.com/danfortunato/surface-diffusion (2022).
27. Fortunato, D. danfortunato/surface-diffusion (v1.0.0). *Zenodo* https://doi.org/10.5281/zenodo.6762738 (2022).
28. Ihrig, E. & Golubitsky, M. Pattern selection with O(3) symmetry. *Physica D* **13**, 1–33 (1984).
29. Henry, M., Hilhorst, D. & Muratov, C. B. A multiple scale pattern formation cascade in reaction–diffusion systems of activator–inhibitor type. *Interfaces Free Bound.* **20**, 297–336 (2018).
30. Camley, B. A., Zhao, Y., Li, B., Levine, H. & Rappel, W.-J. Crawling and turning in a minimal reaction–diffusion cell motility model: coupling cell shape and biochemistry. *Phys. Rev. E* **95**, 012401 (2017).
31. Vanderlei, B., Feng, J. J. & Edelstein-Keshet, L. A computational model of cell polarization and motility coupling mechanics and biochemistry. *Multiscale Model. Simul.* **9**, 1420–1443 (2011).
32. Brauns, F., Weyer, H., Halatek, J., Yoon, J. & Frey, E. Wavelength selection by interrupted coarsening in reaction–diffusion systems. *Phys. Rev. Lett.* **126**, 104101 (2021).
33. Ritoré, M. & Sinestrari, C. *Mean Curvature Flow and Isoperimetric Inequalities* (Springer, 2010).
34. Rubinstein, J. & Sternberg, P. Nonlocal reaction–diffusion equations and nucleation. *IMA J. Appl. Math.* **48**, 249–264 (1992).
35. Ros, A. The isoperimetric problem. *Glob. Theory Minim. Surf.* **2**, 175–209 (2001).

36. Morgan, F. & Johnson, D. L. Some sharp isoperimetric theorems for Riemannian manifolds. *Indiana Univ. Math. J.* **49**, 1017–1041 (2000).

37. Ritoré, M. Constant geodesic curvature curves and isoperimetric domains in rotationally symmetric surfaces. *Commun. Anal. Geom.* **9**, 1093–1138 (2001).

38. Fonda, P., Rinaldin, M., Kraft, D. J. & Giomi, L. Interface geometry of binary mixtures on curved substrates. *Phys. Rev. E* **98**, 032801 (2018).

39. Wigbers, M. C. et al. A hierarchy of protein patterns robustly decodes cell shape information. *Nat. Phys.* **17**, 578–584 (2021).

40. Zhang, Z., Zwick, S., Loew, E., Grimley, J. S. & Ramanathan, S. Mouse embryo geometry drives formation of robust signaling gradients through receptor localization. *Nat. Commun.* **10**, 4516 (2019).

41. Tan, T. H. et al. Topological turbulence in the membrane of a living cell. *Nat. Phys.* **16**, 657–662 (2020).

42. Deneke, V. E., Melbinger, A., Vergassola, M. & Di Talia, S. Waves of cdk1 activity in S phase synchronize the cell cycle in *Drosophila* embryos. *Dev. Cell* **38**, 399–412 (2016).

43. Liu, J. et al. Topological braiding and virtual particles on the cell membrane. *Proc. Natl Acad. Sci. USA* **118**, e2104191118 (2021).

44. Miller, P. W., Stoop, N. & Dunkel, J. Geometry of wave propagation on active deformable surfaces. *Phys. Rev. Lett.* **120**, 268001 (2018).

45. Baker, R. E. & Maini, P. A mechanism for morphogen-controlled domain growth. *J. Math. Biol.* **54**, 597–622 (2007).

46. Gomez, D., Iyaniwura, S., Paquin-Lefebvre, F. & Ward, M. Pattern forming systems coupling linear bulk diffusion to dynamically active membranes or cells. *Philos. Trans. R. Soc. A* **379**, 20200276 (2021).

47. Kirk, B. S., Peterson, J. W., Stogner, R. H. & Carey, G. F. libMesh: a C++ library for parallel adaptive mesh refinement/coarsening simulations. *Eng. Comput.* **22**, 237–254 (2006).

48. Calvo, M., de Frutos, J. & Novo, J. Linearly implicit Runge–Kutta methods for advection–reaction–diffusion equations. *Appl. Numer. Math.* **37**, 535–549 (2001).

49. Miller, P. W. & Dunkel, J. Gait-optimized locomotion of wave-driven soft sheets. *Soft Matter* **16**, 3991–3999 (2020).

50. Miller, P. Source data for 'Forced and spontaneous symmetry breaking in cell polarization'. *Zenodo* https://doi.org/10.5281/zenodo.6774314 (2022).

Author contributions

S.S., L.G. and C.M. designed the research. P.W.M. performed analytical and numerical studies. D.F. developed the numerical method and software. All authors discussed the results and wrote the paper.

Competing interests

The authors declare no competing interests.

Additional information

Supplementary information The online version contains supplementary material available at https://doi.org/10.1038/s43588-022-00295-0.

Correspondence and requests for materials should be addressed to Cyrill Muratov, Leslie Greengard or Stanislav Shvartsman.

Peer review information *Nature Computational Science* thanks Johannes Borgqvist, Anotida Madzvamuse and the other, anonymous, reviewer(s) for their contribution to the peer review of this work. Primary Handling Editor: Ananya Rastogi, in collaboration with the *Nature Computational Science* team.

Reprints and permissions information is available at www.nature.com/reprints.

Publisher's note Springer Nature remains neutral with regard to jurisdictional claims in published maps and institutional affiliations.

Springer Nature or its licensor holds exclusive rights to this article under a publishing agreement with the author(s) or other rightsholder(s); author self-archiving of the accepted manuscript version of this article is solely governed by the terms of such publishing agreement and applicable law.

nature research

Corresponding author(s): Stas Shvartsman, Cyrill Muratov, Leslie Greengard

Last updated by author(s): Jun 28, 2022

Reporting Summary

Nature Research wishes to improve the reproducibility of the work that we publish. This form provides structure for consistency and transparency in reporting. For further information on Nature Research policies, see our Editorial Policies and the Editorial Policy Checklist.

Statistics

For all statistical analyses, confirm that the following items are present in the figure legend, table legend, main text, or Methods section.

n/a	Confirmed	
☐	☒	The exact sample size (*n*) for each experimental group/condition, given as a discrete number and unit of measurement
☐	☒	A statement on whether measurements were taken from distinct samples or whether the same sample was measured repeatedly
☒	☐	The statistical test(s) used AND whether they are one- or two-sided *Only common tests should be described solely by name; describe more complex techniques in the Methods section.*
☒	☐	A description of all covariates tested
☒	☐	A description of any assumptions or corrections, such as tests of normality and adjustment for multiple comparisons
☐	☒	A full description of the statistical parameters including central tendency (e.g. means) or other basic estimates (e.g. regression coefficient) AND variation (e.g. standard deviation) or associated estimates of uncertainty (e.g. confidence intervals)
☒	☐	For null hypothesis testing, the test statistic (e.g. F, t, r) with confidence intervals, effect sizes, degrees of freedom and P value noted *Give P values as exact values whenever suitable.*
☒	☐	For Bayesian analysis, information on the choice of priors and Markov chain Monte Carlo settings
☒	☐	For hierarchical and complex designs, identification of the appropriate level for tests and full reporting of outcomes
☒	☐	Estimates of effect sizes (e.g. Cohen's *d*, Pearson's *r*), indicating how they were calculated

Our web collection on statistics for biologists contains articles on many of the points above.

Software and code

Policy information about availability of computer code

Data collection	All main text data was collected using custom MATLAB (R2021a) code, while the supplement also made use of comparative FEM code created using Libmesh (1.5.1). All code related to our implementation of the DFS method has been added to a community repository alongside this publication (doi:10.5281/zenodo.6812339).
Data analysis	All data was analyzed using custom MATLAB (R2021a) code which has been added to a community repository alongside this publication (10.5281/zenodo.6812339).

For manuscripts utilizing custom algorithms or software that are central to the research but not yet described in published literature, software must be made available to editors and reviewers. We strongly encourage code deposition in a community repository (e.g. GitHub). See the Nature Research guidelines for submitting code & software for further information.

Data

Policy information about availability of data

All manuscripts must include a data availability statement. This statement should provide the following information, where applicable:
- Accession codes, unique identifiers, or web links for publicly available datasets
- A list of figures that have associated raw data
- A description of any restrictions on data availability

All data that support the plots within this paper and other findings of this study are available from the corresponding authors upon request. Figures 2, 3 and 4 have associated raw data which available with this manuscript and in a linked DOI repository (doi:10.5281/zenodo.6774314).

Field-specific reporting

Please select the one below that is the best fit for your research. If you are not sure, read the appropriate sections before making your selection.

☒ Life sciences   ☐ Behavioural & social sciences   ☐ Ecological, evolutionary & environmental sciences

For a reference copy of the document with all sections, see nature.com/documents/nr-reporting-summary-flat.pdf

Life sciences study design

All studies must disclose on these points even when the disclosure is negative.

Sample size	Sample size for Figure 4 was chosen such that the measured standard deviation about each plotted data point was roughly on the order of the average difference in mean values of neighboring points. We found this was sufficient to get a clear picture of the parameter dependence of this plot.
Data exclusions	There were no data exclusions in our analysis.
Replication	All findings in this study can be easily replicated with the code which has been made public.
Randomization	Random initial conditions for all simulations were determined via a script titled randnfun3 which is included in the public repository.
Blinding	All presented quantitative results feature data which is collected and analyzed in an automated fashion by pre-implemented numerical scripts, without notable human intervention. As a result, no special steps are needed to maintain blindness.

Reporting for specific materials, systems and methods

We require information from authors about some types of materials, experimental systems and methods used in many studies. Here, indicate whether each material, system or method listed is relevant to your study. If you are not sure if a list item applies to your research, read the appropriate section before selecting a response.

Materials & experimental systems

n/a	Involved in the study
☒ ☐	Antibodies
☒ ☐	Eukaryotic cell lines
☒ ☐	Palaeontology and archaeology
☒ ☐	Animals and other organisms
☒ ☐	Human research participants
☒ ☐	Clinical data
☒ ☐	Dual use research of concern

Methods

n/a	Involved in the study
☒ ☐	ChIP-seq
☒ ☐	Flow cytometry
☒ ☐	MRI-based neuroimaging